Mycolactone Toxin Membrane Permeation: Atomistic versus Coarse-Grained MARTINI Simulations

Fikret Aydin,[1] Rui Sun,[1] and Jessica M. J. Swanson[1,*]
[1]Department of Chemistry and Institute for Biophysical Dynamics, University of Chicago, Chicago, Illinois

ABSTRACT   Mycolactone, a cytotoxic and immunosuppressive macrolide produced by *Mycobacterium ulcerans*, is the central virulent factor in the skin disease Buruli ulcer. This multifunctional cytotoxin affects fundamental cellular processes such as cell adhesion, immune response, and cell death by targeting various cellular structures. Developing effective diagnostics that target mycolactone has been challenging, potentially because of suspected interactions with lipophilic architectures, including membranes. To better understand the pathogenesis of Buruli ulcer disease, aid in the development of diagnostics, and learn how amphiphiles in general use lipid trafficking to navigate the host environment, we seek to understand the nature of mycolactone-membrane interactions. Herein, we characterize how the two dominant isomers of mycolactone (A and B) interact with and permeate DPPC membranes with all-atom molecular dynamics simulations employing transition-tempered metadynamics and compare these results to those obtained by MARTINI coarse-grained simulations. Our all-atom simulations reveal that both isomers have a strong preference to associate with the membrane, although their mechanisms and energetics of membrane permeation differ slightly. Water molecules are found to play an important role in the permeation process. Although the MARTINI coarse-grained simulations give the correct free energy of membrane association, they fail to capture the mechanism of permeation and role of water during permeation as seen in all-atom simulations.

SIGNIFICANCE   Mycolactone is the sole virulence factor in the neglected tropical skin disease Buruli ulcer. Key outstanding questions are how this toxin invades host cells, is long lived in the host vasculature, evades the secondary immune response, and is difficult to detect with antibodies. Each of these issues could be explained by interactions with lipophilic carriers, including membranes. Using state-of-the-art enhanced sampling methods, we herein calculate permeation free energy profiles, thereby revealing how mycolactone interacts strongly with model lipid membranes. Comparing atomistic to MARTINI coarse-grained simulations reveals the importance of atomistic modeling and properly accounting for hydration during permeation. This work sets the stage for understanding how mycolactone is trafficked and distributed in host systems.

INTRODUCTION

Mycolactone is an exotoxin produced by *Mycobacterium ulcerans* and the central causative agent behind the ne-

glected tropical skin disease called Buruli ulcer (1). The main characteristics of Buruli ulcer disease are extensive tissue destruction (due to the cell death) and a surprisingly low level of pain or inflammation (2,3). The toxin is thought to be secreted in bacterial outer membrane vesicles and then delivered to host cells (4) where it is cytotoxic and immunosuppressive, disrupting various cellular functions such as cytoskeletal organization, cytokine and chemokine expression, and other signaling cascades (5,6). Although multiple cellular targets have been identified, the majority of the toxin's cellular effects can likely be explained by its inhibition of the sec61 translocon (7–9). By binding to the translocon pore, the toxin has been shown to block cotranslational translocation of secretory proteins, leading to numerous downstream consequences. Other cellular targets

include angiotensin II receptors expressed by neurons (10,11) and the Wiskott-Aldrich syndrome protein (WASP) to which mycolactone binds with a 100-fold higher binding affinity than CDC42, the strongest natural activator of WASP (12). Binding of mycolactone causes WASP to open, exposing a domain that activates the Arp2/3 complex (13), which in turn nucleates branched filamentous actin and results in excessive actin branching. Excessive actin branching is associated with abnormal cell adhesion and uncontrolled cell migration that can also induce apoptosis of host cells.

It is unknown why the toxin has so many biological targets or what unifies its multiple effects. One interesting possibility arises from the toxin's expected interactions with membranes. Both angiotensin II receptors and WASP are membrane-associated proteins that have been suggested to be regulated by ordered microdomains that localize and facilitate the assembly of signaling complexes (14–16). Our previous computational work suggested that toxin decreases line tension, thereby disrupting domain formation (17). Recent experimental work confirmed this prediction (14). Using Langmuir monolayers to mimic the plasma membrane, mycolactone was shown to preferentially bind membranes with cholesterol and destabilize the lipid ordered phase, disrupting domain formation and fluidizing the membrane. These findings suggest that mycolactone's influence on membrane reshaping could unify or at least enhance its multiple effects. However, the finding that a single point mutation to the sec61 translocon confers broad resistance to mycolactone indicates that membrane interactions alone do not suffice for its virulence (7,18). It is more likely that membrane interactions play a key role in the toxin's uptake into host cells and long-lived distribution in the host system.

Although treatment regimens exist and are improving (19–29), early detection of Buruli ulcer disease remains a significant challenge. Current diagnostic strategies include microscopic detection of acid-fast bacilli, cultures, PCR targeting specific *M. ulcerans* genes, and histopathology (30). However, none of these strategies are rapid, reliable, or field deployable to the remote locations where they are often needed. Targeting the toxin itself in a diagnostic assay would be ideal and has been identified as a central research aim by the World Health Organization (20). One motivation for this is to distinguish Buruli ulcer from multiple other skin diseases that present similarly in the clinic. Because *M. ulcerans* is the only mycobacterium that produces mycolactone, a diagnostic that targets the toxin will be specific to Buruli ulcer disease. Despite numerous efforts toward this goal however, rapid diagnostic assays targeting mycolactone have yet to be identified. One promising advance was the development of mycolactone-specific monoclonal antibodies (31). Unfortunately, these antibodies have only proven to be effective and/or neutralizing if they are preequilibrated with the toxin before exposure to host cells. One possible explanation for this, which is consistent with the toxin's amphipathic (or

amphiphilic) structure, is that that toxin is hidden from tracking antibodies because of association with lipophilic carriers such as membranes. Although early imaging studies with boron-dipyrromethene-labeled mycolactone reported passive diffusion across membranes and uptake into the cytoplasm (32), these images are also consistent with uptake into the endoplasmic reticulum, which would be consistent with its confirmed targeting of the sec61 translocon (7–9). Furthermore, association with other lipophilic structures like high-density lipoproteins would explain the toxin's long-lived lifetime in the host system and ability to travel far from the site of infection in the host serum. In fact, association with high-density lipoprotein was recently confirmed experimentally (33). This is promising for the development of blood-based diagnostic assays, assuming the toxin can be distinguished from its lipophilic carriers.

In this work, we aim to further characterize the nature of mycolactone-membrane interactions to better understand its mechanism of host cell penetration and distribution in the host environment, factors highly relevant to the toxin's pathogenicity and the design of effective diagnostics. We are additionally testing the use of our recently developed transition-tempered metadynamics (TTMetaD) method to characterize membrane permeation of a relatively large molecule at the all-atom level and carefully comparing these results to those from coarse-grained (CG) MARTINI simulations. Following up on the work of López et al. (17), we have herein used both CG and all-atom molecular dynamics (MD) simulations employing TTMetaD to characterize the association of the toxin with dipalmitoylphosphatidylcholine (DPPC) membranes. We calculate membrane permeation free energy profiles for both isomers A and B, which exist in a 60:40 ratio. Our simulations show that 1) the toxin has a strong preference for lipid phase with a 14–17 kcal/mol driving force to associate with a DPPC membrane; 2) the mechanism of permeation and binding energy differ slightly for the A (~16 kcal/mol) and B (~14 kcal/mol) isomers, with B preferring to associate with the glycerol groups; and 3) water facilitates permeation by associating with the polar tails of the toxin. Comparisons with the MARTINI simulations demonstrate how the CG approach gets the free energy of membrane association approximately correct, in concert with the parameterization procedure, but differs significantly in the mechanism of permeation and involvement of water. The insights gained are discussed in the context of how mycolactone-lipid interactions may influence the toxin's association with and trafficking via membranes (i.e., how is it taken up into the endoplasmic reticulum so quickly?), as well as its distribution in the host environment (how might it be transferred to other lipophilic carriers?). Not only will our continued understanding of this toxin-membrane dynamic be useful in the development of diagnostics and adjunctive treatment approaches for Buruli ulcer disease, but it also serves as a fascinating model system of amphipathic-host interactions and lipid trafficking.

METHODS

All-atom MD simulation

In our all-atom MD simulations, there are 50×2 DPPC molecules solvated with $\sim$6000 water molecules (hydration ratio of 60), expanding to a roughly 5.6×5.6-nm region laterally (x-y directions), a size that is too large for a fully extended mycolactone ($\sim$3 nm) to interact with itself across periodic boundaries. The thickness of the simulation box (z direction) is $\sim$10 nm. To compare our results with the previously published results of López et al. (17), we adopted the same MD simulation parameters for mycolactone from that work, which were developed with the general Amber force field (34,35) and restrained electrostatic potential charges. To validate these parameters, we compared them to those generated with the general automated atomic model parameterization protocol (36) and found them to be reasonably consistent. The DPPC molecules are modeled using an Amber-based force field (37) with corrections to balance the hydrophilic and hydrophobic forces (38). The water molecules are modeled using TIP3P force field (39). The initial structure of the DPPC lipid bilayer was prepared using CHARMM-GUI membrane builder (40) and equilibrated for 250 ns in water, and its thickness and area per headgroup were compared to the experimental value to confirm the bilayer had been equilibrated properly. Based on the last 100 ns of the equilibration, the all-atom simulations of the DPPC lipid bilayer had an area per headgroup of 62.1 ± 1.0 Å^2 and a thickness (measured as the z distance between the phosphate atoms in two monolayers) of 38.7 ± 0.5 Å. This compares well with the experimental values of 64 Å^2 and 38.5 Å (41), as well as previous simulations of DPPC alone using this force field (42). One mycolactone molecule was then added into the bulk water in a random orientation. Thermostats (323 K) using velocity rescaling with a stochastic term (43) were applied to the lipid bilayer and the rest of the system separately with a coupling time of 1 ps. A semi-isotropic Berendsen barostat (44) (isotropic in the x and y directions, but independent in the z direction) was applied to control the pressure of the system with a coupling time of 5 ps. The cutoff distance for the short-range interaction list was 1.0 nm, which was updated every 10 steps. The long-range electrostatic interactions were computed using fast smooth particle mesh Ewald (45) with a real space cutoff of 1.0 nm, and all hydrogen bonds were constrained by linear constraint solver (46). There were four replicas of $\sim$3 μs of TTMetaD simulations (integration time step: 2 fs) for both mycolactone A and B, with the initial velocities randomly sampled from a Boltzmann distribution. The equilibrated DPPC lipid bilayer was used as the initial structure of the toxin-membrane system. In addition, the same simulation protocol (i.e., the cutoffs, thermostat, barostat) was used to simulate both membrane-only and toxin-membrane systems. The all-atom MD simulations were carried out using GROMACS 2016.4 (47) patched with a version of PLUMED 2.4.1 (48) to perform TTMetaD (publicly available in PLUMED version 2.4 and beyond). In addition, all-atom simulations of mycolactone B were run in the absence of any biasing force to verify the convergence of the role of hydration during permeation. The toxin was placed in the bulk solvent and allowed to associate with the membrane for a total of 500 ns of simulation. There were four replicas of 500 ns of unbiased all-atom simulations. The area per lipid in these replicas was 61.0 ± 1.0 Å^2, which is minimally altered from the membrane-only system.

TTMetaD

Because membrane permeation is generally a slow process compared to the timescales accessible in MD simulations, enhanced sampling methods must be used. We have employed a variant of metadynamics (MetaD) (49–51) in which a bias energy (V_G) is added to the Hamiltonian of the system along the simulation through a small number of preselected collective variables (CVs) that represent the system of interest. The bias energy usually takes the form of the summation of Gaussian functions (Eq. 1), which are centered at the previously visited configuration in CV space, with a width of a tiny fraction of the CV scale.

$$V_G(s,t) \ = \ \int_0^t dt' w \exp\left[-\sum_{i=1}^d \frac{(S_i(R) - S_i(R(t')))^2}{2\sigma_i^2} \right]. \quad (1)$$

In the above equation, σ is the width of the Gaussian function and w stands for the bias energy incremental rate, that is, the height of the Gaussian functions (w_0) divided by its deposition stride (τ). $S_i(R(t'))$ is CV value evaluated from the configuration of the system at time t' with the index i representing the ith CV. As a result of the bias energy, the system is discouraged from revisiting the previously visited point, pushing it away from local energy minima such that it can explore higher-energy regions in CV space. Eventually, the motion of the system in CV space becomes diffusive and ergodic, indicating the bias energy has offset the "resistance" of the system. As a result, the underlying free energy of the system can be estimated as the negative of the MetaD bias energy. This approach, originally introduced in 2002 (49), is often regarded as nontempered MetaD today because the height of the Gaussian in Eq. 1 remains constant throughout the simulation. Although nontempered MetaD is generally effective in exploring CV space, the bias energy oscillates around the true underlying potential of the mean force (PMF) instead of converging asymptotically, in contrast to the fact that the PMF is a time-independent property. Calculating time average of the bias energy from nontempered MetaD (only after the motion of the system becoming diffusive) has been proposed as a solution to this convergence issue, but practically, we have found that this either shows false convergence or destabilizes the simulation because of too much bias energy being added (52,53).

The incremental bias additions (i.e., w in Eq. 1, depending on the height of individual Gaussian, w_0) need to approach zero to achieve the true convergence of the bias energy. Well-tempered metadynamics (WTMetaD) (54) accomplishes this by replacing the time-independent incremental bias additions (w) with a time-dependent quantity, $w(t)$:

$$w(t) \ = \ w_0 \exp\left[-\frac{V_G(s,t)}{k_B \Delta T} \right]. \quad (2)$$

The bias energy incremental rate decreases exponentially with respect to the local bias energy. The parameter ΔT tunes the amount of decrement and is chosen before the simulation. In principle, WTMetaD has been proven to converge the bias energy asymptotically to a linearly scaled inverse of the underlying free energy (55). Despite the success of WTMetaD, it presents a trade-off between the exploration and the converging in WTMetaD: a fast-growing bias potential (with large ΔT) leads to a noisy bias energy, hindering the convergence; a slow-growing (with small ΔT) leads to a smooth bias potential, hindering the exploration. It has been suggested that ΔT should be chosen according to the largest free energy barrier so that $(\Delta T + T)k_B$ has the same order of magnitude as the barrier (54). However, the barrier height is usually the most interesting feature of the system and is often unavailable; therefore, the efficiency of WTMetaD can sometimes be limited considerably.

Converging like WTMetaD, TTMetaD (56) overcomes the aforementioned trade-off by tempering the bias energy cleverly with respect to overall progress of the MetaD sampling. Namely, a global property V^*, the minimal bias on the maximally biased path among all the continuous paths $s(\lambda)$ connecting all of the preselected points in the CV space, replaces the local bias energy V_G (Eq. 2):

$$w(t) \ = \ w_0 \exp\left[-\frac{V^*(s(\lambda),t)}{k_B \Delta T} \right]. \quad (3)$$

In TTMetaD, the preselected points are the basins on the underlying free energy surface, separated by a significant barrier. Intuitively, V^* can be understood as the amount of the bias energy needed for the least-likely point in the CV space to be sampled, usually corresponding to the transition state

(TS) region. The $V*$ remains zero before the basins are connected through TS; thus, TTMetaD explores with a full Gaussian. Once the TS region has been sampled, TTMetaD can afford a more aggressive tempering (small ΔT) of the bias energy incremental rate to converge the simulation. TTMetaD has demonstrated its advantages of converging rapidly and asymptotically in various studies of complicated biophysical systems (52,53). The two-dimensional (2D) PMF is estimated from the reverse of the average of the bias energy from four independent replicas and then diagonally symmetrized with respect to the center of the membrane and toxin orientation. This method has previously demonstrated its efficiency in converging TTMetaD simulations, especially for the lipid bilayer permeation. The minimal free energy path (MFEP) on the 2D PMF (Fig. 4, *black curve*), which represents the most common pathway in a large ensemble of the permeation processes, was calculated with a zero temperature string method (57). One-dimensional (1D) PMF is directly obtained by using the average MFEP from four independent replicas (58).

CG MD simulation

In principle, using a CG approach like MARTINI (59) could enable simulations of mycolactone interacting with membranes at much larger length scales and longer timescales. Thus, our intention in comparing our all-atom MD results to those from MARTINI is to verify its reliability in modeling this complicated toxin-membrane interaction. To make as clear of a comparison as possible, the same methods were employed and the same system size was used as those in the all-atom MD simulations (adjusting for the MARTINI CG water bead representing four water molecules). We focused the comparison on the permeation of mycolactone B only. The MARTINI CG force field parameters were adapted from the López et al. (17) work in which the MARTINI CG representation of mycolactone B was obtained from the insane protocol (60). After equilibration, the dimension of the MARTINI CG simulation box was ~5.5 × 5.5 × 6.6 nm. Although the length along the z direction decreased significantly from the all-atom scale, this was still deemed sufficient for the characterization of permeation. The hydration ratio of the MARTINI CG simulations was ~10 water beads per lipid, which is consistent with the previous MARTINI CG simulations of lipid membranes (61–63). The MARTINI simulations of the DPPC lipid bilayer had an area per headgroup of 61 ± 1.1 Å^2 and a thickness of 40 ± 0.6 Å (based on the distances between phosphate groups in two monolayers). This compares well to previous MARTINI simulations of pure DPPC (64). The thermostat, barostat, and long-range electrostatic interactions were kept consistent with those used in the all-atom MD simulations. Various short-range interaction cutoff distances and neighbor list update frequencies were tested, and final values of 1.2 nm/updating every 10 steps were chosen for the stability of the simulation. These are different from those previously used (17). The previous MARTINI CG simulations (17) employed a shorter nonbonded interaction cutoff (0.9 nm), as well as tighter thermostat and barostat couplings, and frequent neighbor list updates, which caused system instability and significant energy leak issues (when checked with NVE simulations), similar to those reported in a previous work (65). There were six replicas of 20 μs (dummy integration time step: 20 fs) for the TTMetaD MARTINI CG simulations.

CVs

Whereas all of the interactions between the toxin, membrane, and water are consistently represented by the force fields described above, enhanced sampling focuses on specific, relevant degrees of freedom (CVs) to speed up the process of interest (permeation in this case). In MetaD, the bias energy is deposited into CV space to accelerate exploration of the free energy landscape. In general, the CV needs to capture the process of interest (e.g., a reaction coordinate for a chemical reaction), delineating between the starting and ending states (e.g., reactant and product). Ideally, it should

also capture the slow degrees of freedom that limit progression from the start to end state. Using TTMetaD, we have studied the permeation of small organic molecules though lipid bilayers and found that at least two CVs are often necessary: one that describes the center of mass translation of the permeant through the membrane and another that describes molecular reorientation during permeation. Because mycolactone is a relatively large and flexible molecule, both the center of mass of the whole molecule and the center of mass of the lactone ring were tested as CVs to define the translation of the permeant; the latter was chosen because it demonstrated faster convergence, whereas the former failed to delineate between a wide range of configurations with slow interconversion, thereby limiting convergence. The orientation CV was defined as the angle between the vector connecting the hydroxyl groups on the end of the northern and southern tails and the vector normal to the lipid bilayer. An illustration of the two CVs is shown in Fig. 1. The same CVs are defined for the MARTINI CG simulations through the corresponding beads.

RESULTS AND DISCUSSION

Interconversion between mycolactone A and B

Mycolactone is a polyketide composed of an invariant 12-membered lactone ring with two highly unsaturated acyl side chains (Fig. 2, *top panel*). The shorter side chain (called the "Northern" chain by convention) is invariant, whereas the longer ("Southern") chain varies in different congeners of mycolactone. The most cytotoxic and common congener is mycolactone A/B (in vitro), which exists in two isomeric forms in a ratio of 60:40 (A/B) under common laboratory conditions and light. We sought to perform our all-atom simulations on both isomers to see if, within the limited accuracy of the force field and simulation techniques, the permeation process differs. We first considered interconversion between the two isomeric forms. One mycolactone B molecule was solvated with 4400 water molecules in a simulation box with a volume of 133 Å^3. An unbiased simulation was run for 1.6 μs by following the same MD simulation protocol as the one described in Methods. Although the dihedral angle of the single bond (4-5-6-7) is flexible, leading to the conformational change between mycolactone B and B′ (Fig. 2), the 3-4-5-6 (double bond) dihedral angle distribution from the simulation shows it is very stable, as
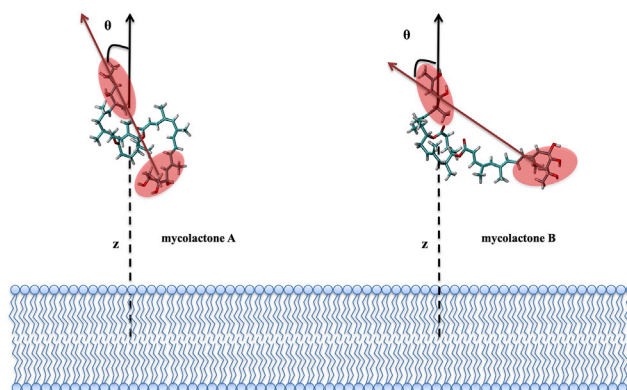

FIGURE 1 Definition of CVs for mycolactone A/B permeation through a DPPC lipid bilayer. To see this figure in color, go online.
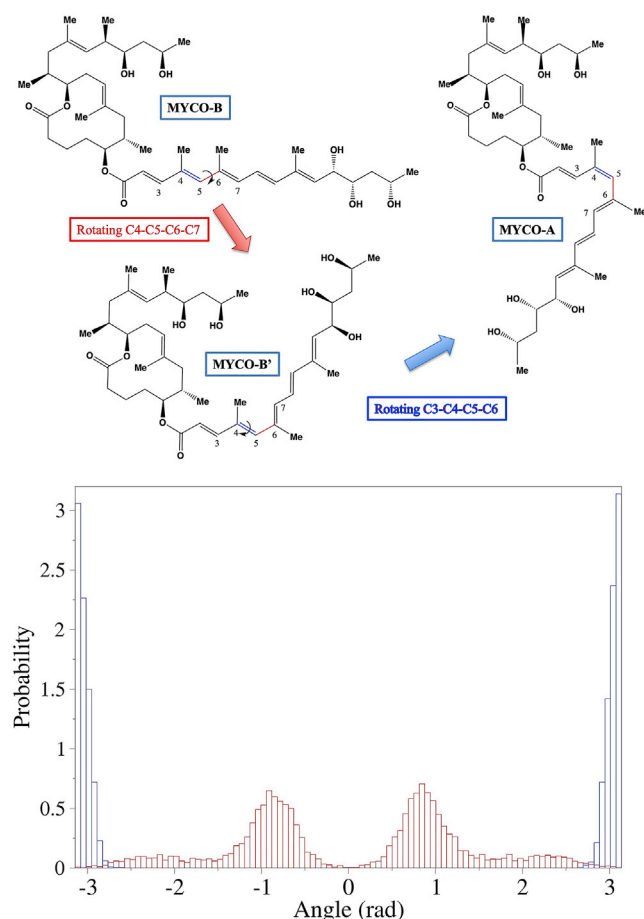
FIGURE 2 Top panel: the conformation of mycolactone A and B. The bottom panel shows the normalized distribution of dihedral angle 3-4-5-6 (*blue*) and 4-5-6-7 (*red*) from mycolactone B and water simulation. To see this figure in color, go online.

FIGURE 3 Top panel: all-atom (*left*) and coarse-grained (CG) (*right*) structures of mycolactone. The northern tail, southern tail, and lactone ring are orange, yellow, and purple, respectively. Oxygen atoms of mycolactone in all-atom structure are red. The bottom panel shows the DPPC membrane structure from all-atom simulations. The upper monolayer is colored based on different lipid regions: hydrophobic tail (*yellow*), glycerol (*blue*), phosphate (*red*), and choline (*orange*). To see this figure in color, go online.

expected, on a microsecond timescale. Therefore, the permeation of mycolactone A and B are modeled separately in atomistic simulations in this study.

Permeation PMF from all-atom simulations

The DPPC membrane and mycolactone molecule (in all-atom and CG representation) are depicted in Fig. 3. The 2D PMF of the permeation of mycolactone B through DPPC lipid bilayer is shown in Fig. 4, with the inserted snapshots illustrating representative configurations. Our results confirm the strong affinity between mycolactone and lipid bilayers, reported by both experiments and MARTINI CG simulations (14,17). It is important to note that multiple permeations of the toxin from both sides of the membrane were observed during the TTMetaD simulations.

The MFEP demonstrates how the permeation process is dominated by hydrophobic-hydrophilic interactions between mycolactone and DPPC lipids. When mycolactone approaches the lipid bilayer, the two hydrophilic tail ends (including two and three hydroxyl groups on the northern
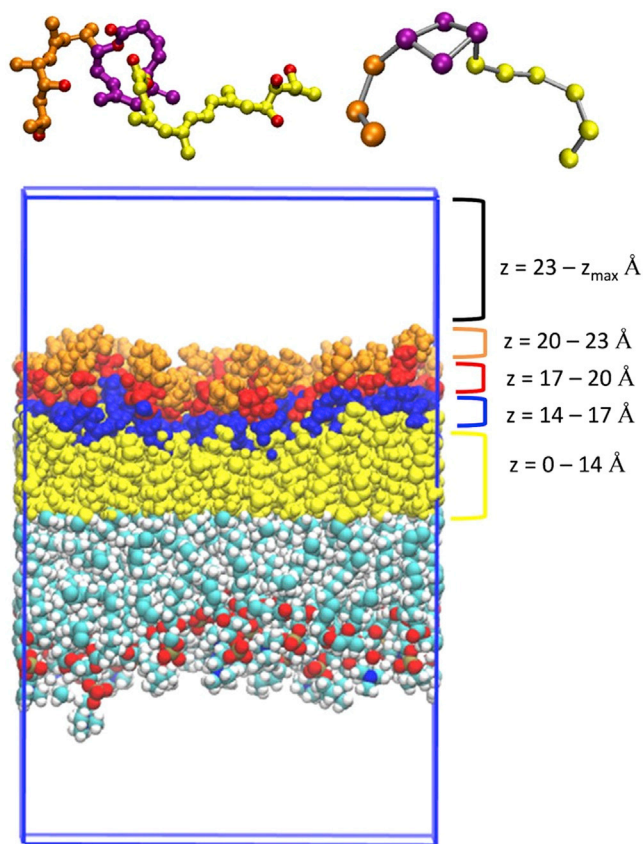
and southern tails, respectively) interact with the hydrophilic headgroups of the lipid bilayer (Fig. 4, *configuration 1*). This mycolactone-tail/DPPC-head interaction is strongly favored in free energy and remains stable as the toxin moves into (and out of) the bilayer; therefore, the orientation CV value (θ) does not vary significantly from -4 to -1 nm (and 1–4 nm). As the permeation continues, the hydrophobic lactone ring submerges into the tail groups of the lipid bilayer (Fig. 4, *configuration 2*). This configuration corresponds to the lowest free energy on the 2D PMF. To permeate to the other side, the toxin flips, keeping hydrophobic lactone ring in the lipid tail region and swapping the hydrophilic toxin tails to interact with the headgroups on the other lipid leaflet. Finally, the lactone ring is pulled from the tail group region to finish the permeation process. The preference of the toxin tails to interact with the polar headgroups is also apparent in the 1D free energy profile of the MFEP (Fig. 6), which shows a slight increase in the free energy in the middle of the membrane (Z = 0.7–0 nm). It is
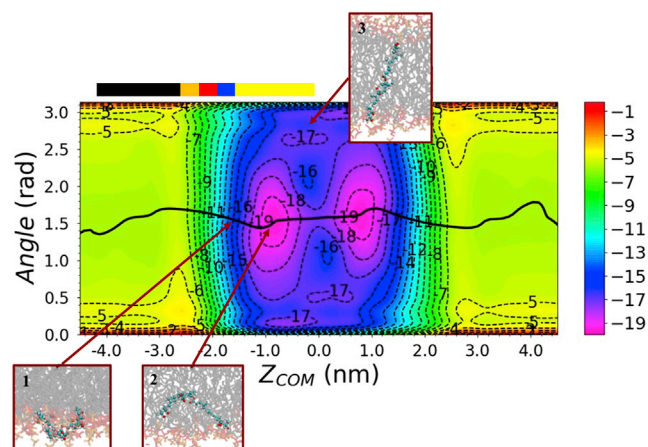
FIGURE 4 2D PMF of mycolactone B permeation through DPPC lipid bilayer from all-atom simulations. The black line represents the MFEP, and the inserted figures depict the representative configurations. The toxin is colored by atom type, whereas the DPPC headgroups, glycerols, and tails are colored with orange, red, and gray, respectively. The membrane spans $-2.0 < Z < 2.0$ nm. The color bar corresponds to the colored regions of the DPPC membrane shown in Fig. 3. The energy is shown in units of kilocalories per mole. To see this figure in color, go online.
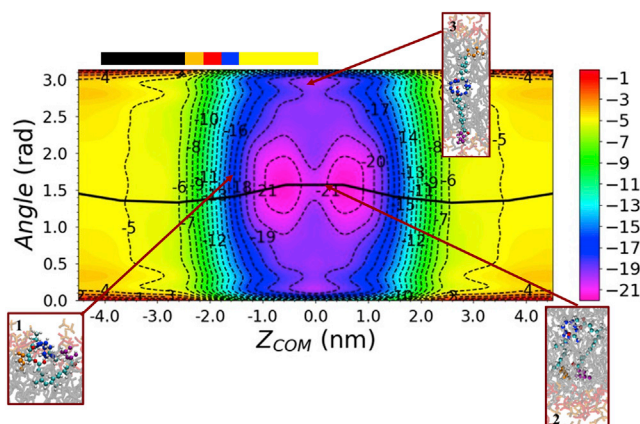

FIGURE 5 2D PMF of mycolactone A permeation through DPPC lipid bilayer from all-atom simulations. The black line represents the MFEP, and the inserted figures depict the representative configurations. The northern tail, southern tail, and lactone ring are colored with orange, purple, and blue, respectively. The DPPC headgroups, glycerols, and tails are colored with orange, red, and gray, respectively. The color bar corresponds to the colored regions of the DPPC membrane shown in Fig. 3. The energy is shown in units of kilocalories per mole. To see this figure in color, go online.

important to point out that the stretched configuration of mycolactone, where the northern and southern tails interact with opposing leaflets (Fig. 4, *configuration 3*), corresponds to a high free energy, disfavored configuration. This is in contrast to the previous MARTINI simulations showing the extended configuration as a favored metastable minimum and suggesting the permeation process involved such an extension as the toxin passes from one side of the membrane to the other (17).

The permeation of mycolactone A through the DPPC bilayer shows a very similar PMF (Figs. 5 and 6) as the permeation of mycolactone B, indicating a similar mechanism. There is a small difference in the binding energies of two isomers during the permeation. Mycolactone A has a stronger binding affinity to the lipid bilayer and smaller energy penalty when the toxin flips from one leaflet to the other. This is also apparent in the 1D free energy profile (Fig. 6), which shows that mycolactone A has a deeper energy minimum and less free energy increase in the middle of the membrane compared to mycolactone B. This can be attributed to a structural difference. With the rotation of a single bond, the two hydrophilic tails in mycolactone A can flip around to hydrogen bond to each other. This better satisfies the polar tail interactions making it easier for the toxin to pass into the lipid tail region and results in stronger binding affinity between isomer A and lipid bilayer because of the minimization of unfavorable interactions between hydrophobic lipid tail region and hydrophilic tails of the toxin. Similar to mycolactone B, the stretched configuration remains unfavorable for mycolactone A (e.g., Fig. 5, *configuration 3*).

The role of hydration in mycolactone membrane permeation

It is intriguing to focus on the role of water during the permeation of mycolactone. As shown in the permeation PMFs of both isomers, the most favored (lowest in free energy) configurations minimize the hydrophobic-hydrophilic interactions: the highly hydrophobic lactone ring is buried in the hydrophobic lipid tails, and the hydrophilic tails are stretching out to the hydrophilic lipid headgroups and/or interacting with water molecules. We first analyzed the number of water molecules interacting with mycolactone
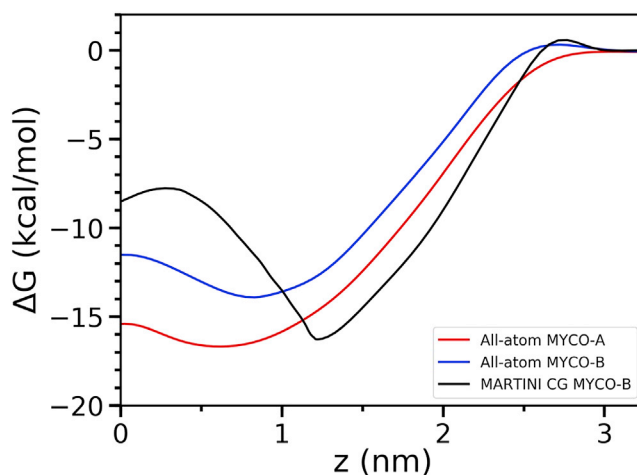

FIGURE 6 1D free energy profiles of the permeation of mycolactone B (atomistic and MARTINI CG) and mycolactone A (atomistic) with respect to the insertion depth of the lactone ring into the lipid bilayer. Error bars (0.2–3 kcal/mol) are not shown for clarity. The energy is shown in units of kilocalories per mole. To see this figure in color, go online.

as a function of the z distance of the lactone ring to the membrane center in the unbiased (mycolactone B) and biased all-atom (mycolactone A and B) simulations, as well as the biased MARTINI CG (mycolactone B) simulations. In the unbiased simulations of mycolactone B, the toxin enters the membrane (at 290, 65, 210, and 180 ns in four replicas) because of its amphipathic structure and spends the remaining simulation time inside the membrane (predominantly in the region of the PMF minimum; 5 Å $\leq Z_{COM} \leq$ 12 Å). The toxin explores the conformations corresponding to the minimal free energy region shown in Fig. 4 (*panels 1 and 2*). A water molecule is considered to be interacting with mycolactone if the center of mass (COM) distance between the oxygen atom of water and any oxygen atom of mycolactone is less than or equal to 3.04 Å for all-atom simulations. The 3.04 Å cutoff corresponds to the sum of van der Waals radii of two oxygen atoms, which we observed to capture the contacts between water molecules and mycolactone well. In concert, a water bead is considered to be interacting with mycolactone if the COM distance between the water bead and any bead of mycolactone is less than or equal to 4.9 Å for MARTINI CG simulations. For MARTINI CG simulations, the effective size of particles is $\sigma = 4.7$ Å (except ring-like molecules, which have a σ of 4.3 Å). The 4.9 Å cutoff was selected to be the sum of the effective size of particles and a padding distance, and we found that this cutoff works well to capture the water coordination of mycolactone in MARTINI CG simulations. The probability distributions of the number of water molecules interacting with mycolactone A and B for biased and unbiased all-atom simulations are all in good agreement (see Fig. 7). Mycolactone continues to interact with water molecules when the lactone ring is near the center of membrane ($z = 0$). However, there is a striking difference between the hydration profiles of all-atom and MARTINI CG simulations. Contrary to the all-atom simulations, the MARTINI mycolactone has a very low probability of interacting with a water bead when the lactone ring moves through the center of membrane. To better understand where these coordinating waters were in the membrane, we next analyzed the position distributions of coordinating water molecules as a function of the z position of the lactone ring. The position distribution of water molecules is obtained by calculating the z distance between each water molecule interacting with mycolactone and the center of membrane (Fig. 8). Similar to the number distributions of water molecules, the position distributions in unbiased and biased all-atom simulations of mycolactone B are in a good agreement with each other. The distribution of the unbiased all-atom simulation is not uniform because the toxin quickly penetrates into the membrane and spends most of the time inside the lipid bilayer. An interesting subtle difference is that the biased simulations have a wider distribution of water positions, mostly associating with water farther away from and to a lesser degree pulling water farther into the center of membrane as compared to the unbiased simulation. This suggests that hydration itself is a slow degree of freedom that is not exhaustively sampled in the TTMetaD simulations. However, the difference is so slight that explicit sampling of a hydration CV is not expected to change the free energy profile significantly. Importantly, both the unbiased and biased all-atom simulations demonstrate deep penetration of water molecules with the insertion of mycolactone into the membrane. Thus, the penetrating water molecules play an important role in the permeation process, compensating for lost hydrophilic interactions. The convergence of the unbiased all-atom simulations was checked by comparing four replicas and showing agreement in the penetration of water molecules. Block averaging the last 100 ns of simulation showed that the number of water molecules penetrating the membrane (Fig. 7, *upper left*) was ~2.55 with a variance of only 0.5 water molecules between replicas, whereas the variance over time was 1.5 water molecules (Table S1). Thus, the penetration of water molecules is reasonably fast compared to toxin permeation, which is consistent with the results in the biased all-atom simulations. Similar to mycolactone B, mycolactone A pulls water molecules deeply into the lipid tail region (see Fig. 8, *right panel*). The representative configurations of each system shown in Fig. 9 demonstrate the water coordination and structures of the isomers A and B in all-atom MD and MARTINI CG simulations. Moreover, the water molecules are pulled deeper into the lipid tail region when the toxins take more compact configurations (Video S1).

In contrast, the position distribution of water beads in the biased MARTINI CG simulations is quite different (Figs. 8 and 9, *middle panel*). When the lactone ring is near the
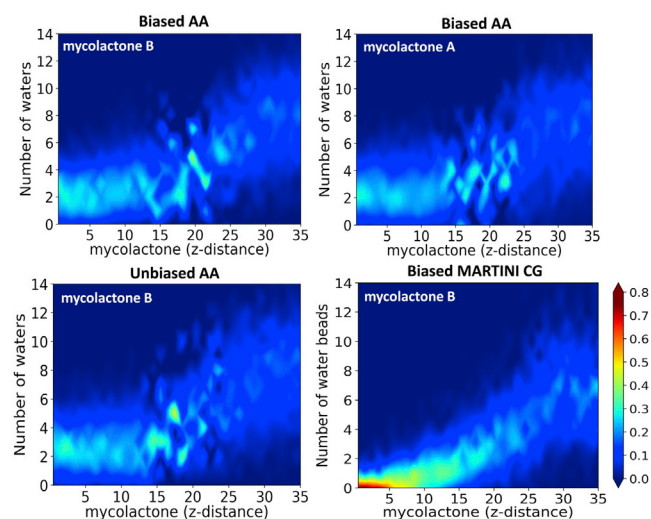

FIGURE 7 Probability distributions of number of water molecules interacting with mycolactone with respect to the insertion depth of the lactone ring into the lipid bilayer from unbiased and biased all-atom simulations and biased MARTINI coarse-grained (CG) simulations. To see this figure in color, go online.
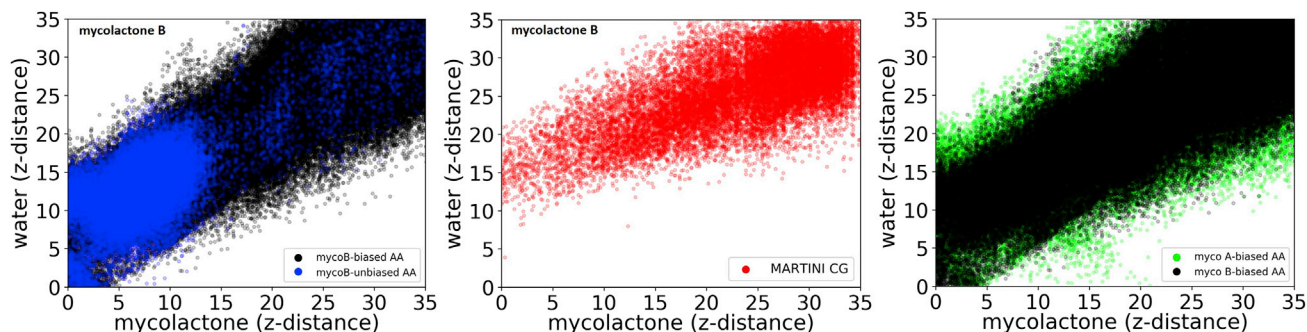
FIGURE 8 Position distributions of water molecules/beads interacting with mycolactone with respect to the insertion depth of the lactone ring from unbiased and biased all-atom simulations and biased MARTINI CG simulations. To see this figure in color, go online.

center of membrane ($z = 0$), the water beads are around or just below the lipid headgroup region ($z = 10–20$ Å) revealing no deep penetration of MARTINI water beads. As discussed below, this is a likely contribution to the free energy barrier close to the membrane center in the MARTINI PMF.

To check whether the hydration ratio in the MARTINI CG simulations has any effect on the water penetration, unbiased MARTINI simulations with small and large hydration spaces were performed. The depth of the penetrating waters in the hydration profiles look almost identical as shown in Fig. S1, verifying that our conclusions on water penetration are not artifactual. The profiles look different in the water region because in the unbiased MARTINI CG simulations, mycolactone quickly penetrates into the lipid bilayer and

spends the rest of the simulation inside the bilayer; thus, there is scarce data in the water region in Fig. S1. In contrast, the hydration profiles in Fig. 8 have abundant data in the water region because they were obtained from biased MARTINI CG simulations in which toxin permeates in and out of the lipid bilayer many times. The relevant comparison, however, is the depth of penetrating water molecules in Figs. S1 and 8 rather than the overall shapes of the hydration profiles.

Impact on lipid packing

To better understand mycolactone's disruptive effect on the membrane, the tail order parameters of the DPPC lipids in the presence and absence of isomers A and B were measured. The tail order parameter (S_{CH}) was calculated
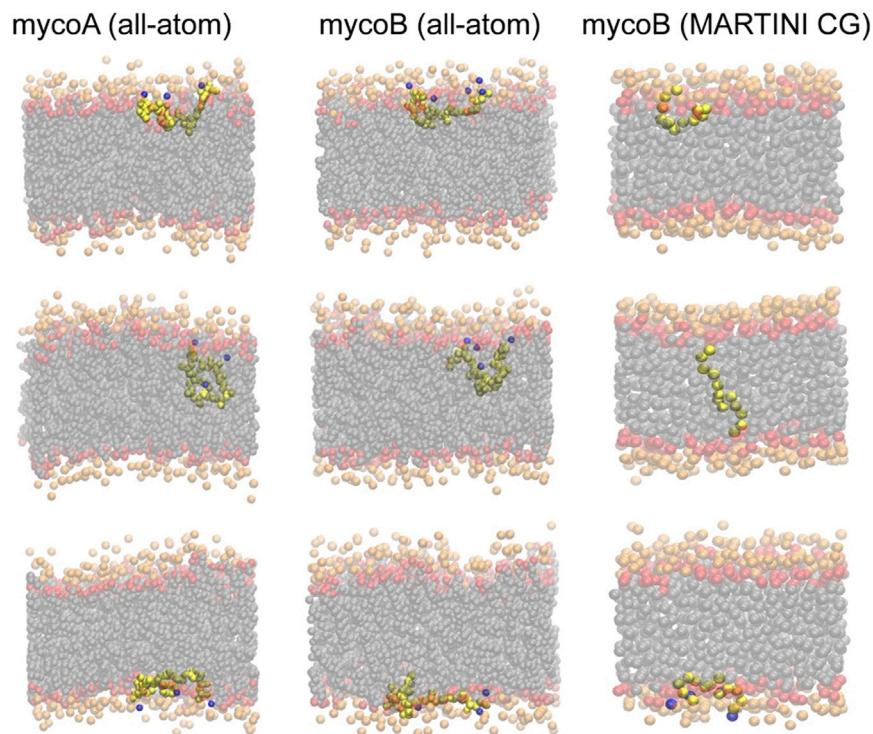

FIGURE 9 The snapshots depict the representative configurations from all-atom simulations of mycolactone A and B (the *left* and *middle columns*) and from MARTINI CG simulations of mycolactone B (the *right column*). The mycolactone and water molecules are colored with yellow and blue, respectively. The DPPC headgroups, glycerols, and tails are colored with orange, red, and gray, respectively. To see this figure in color, go online.

(Eq. 4) by measuring the angle between the vectors of bilayer normal and C-H bond in the lipid (θ) using the following equation:

$$S_{CH} = 3\cos^2\theta - 1/2. \qquad (4)$$

This analysis was done in the biased all-atom simulations of toxin permeation through DPPC as well as the unbiased all-atom simulations of mycolactone B and pure DPPC. The angle was averaged over simulation time and the lipids molecules in the both leaflets of the bilayer to calculate S_{CH} for the whole bilayer. The effect of mycolactone on the order parameter was investigated by averaging over all the lipids that are within 5 Å of mycolactone. Lastly, the order parameters per leaflet were calculated by averaging over the lipids either in the toxin-containing leaflet or in the opposite leaflet. The comparison of the tail order parameters for these different cases is shown in Fig. S2. A noticeable reduction in the lipid tail order parameters was observed for the lipid molecules in the neighbor of mycolactone, which could facilitate the increased water penetration into the membrane with the permeation of mycolactone. A similar reduction was also found in the unbiased simulations of DPPC in the presence of mycolactone B. Moreover, no significant difference was found between the effects of isomers A and B on the lipid tail order parameters, which is consistent with the fact that both isomers A and B pull a similar amount of water molecules into the center of membrane. Interestingly, we find that the order parameters in the toxin-containing leaflet are increased overall (despite the decreased order within 5 Å of the toxin) compared to both the opposite leaflet and the membrane-only simulations. The increased order is consistent with a decrease in the area per lipid, assuming the toxin takes the space of ~2 lipids, to 59.8 ± 1.3 Å^2 in the toxin-containing leaflet compared to 62.1 ± 1.0 Å^2 in the membrane-only system and 62.2 ± 1.3 Å^2 for the less ordered, opposite leaflet (66). The tail order parameters of the opposite leaflet are close to those of the membrane-only system, consistent with the similar area per lipids observed in both cases. The altered lipid packing in the presence of the toxin could induce some degree of tension in our simulations, but we do not expect a significant effect of tension because the mismatch in the area per lipid between two leaflets is small.

Comparison with the MARTINI CG simulation

CG simulations can extend the accessible temporal and spatial scale of molecular modeling, which is sometimes essential to connect with the biological process of interest. However, the accuracy of CG models, especially for molecules they were not originally parameterized for (e.g., organic molecules like mycolactone), is often unknown. To confirm a CG simulation is trustworthy, it is generally

essential to verify the accuracy of a CG model by comparing it to more detailed models and experimental data. In addition, such comparisons can be useful in improving CG methods. Herein, we compare the permeation PMFs and mechanisms of mycolactone B through DPPC lipid bilayers from MARTINI CG and all-atom simulations.

As discussed in the methodology section, the MARTINI CG system was directly coarse grained from the all-atom system, consistent with a previous publication (17). In contrast to that work, the methods used herein are consistent with the methods used for our all-atom simulations to provide as robust of a comparison as possible. TTMetaD was employed to calculate the permeation PMF with exactly the same CVs (after coarse graining) as in Fig. 1. The converged 2D PMF is depicted in Fig. 10, and the 1D free energy profile is in Fig. 6. Compared to the previously published PMF, our PMF shows differences in shape (less stabilization at Z = 0 and smoother transitions) and thermodynamics (ΔG for membrane association of -16 kcal/mol herein vs. -12 kcal/mol previously), which we attribute to treatment of cut off interactions and methods used to sample the PMF.

Comparing our all-atom simulations to our MARTINI simulations, we find that the CG model also predicts a strong driving force for membrane association and affinity for the toxin tails to interact with the lipid headgroups, although this interaction localizes at Z = 1.3 nm as opposed to 0.7 nm as it did in the all-atom simulations (Fig. 6). Again, this optimizes the hydrophobic-hydrophilic interactions. However, the differences are very clear: the MARTINI CG model predicts a barrier for the toxin to pass through the lipid tail region and a metastable fully stretched configuration (Fig. 10, *red circles*) where the two tails of the mycolactone molecule interact with the headgroups on opposing leaflets.
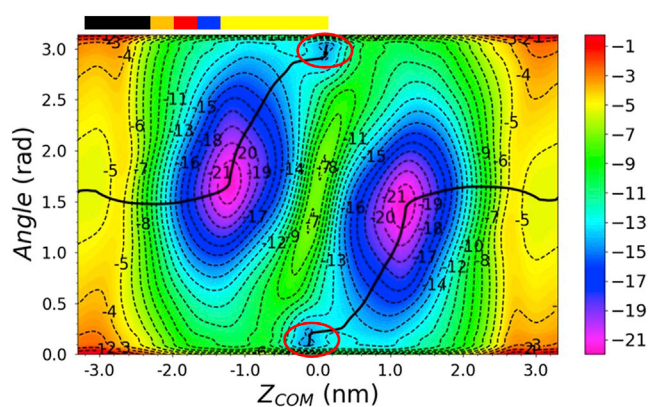

FIGURE 10 2D PMF of mycolactone B permeation through DPPC lipid bilayer from MARTINI CG simulations. The black line represents the MFEP. The red circles illustrate the configurations in which mycolactone is fully stretched to headgroups of both leaflets, corresponding to configuration 3 in Figs. 4 and 5. The color bar corresponds to the colored regions of DPPC membrane given in Fig. 3. The energy is shown in units of kilocalories per mole. To see this figure in color, go online.

This configuration is strongly disfavored according to the all-atom simulation (Fig. 4, *configuration 3*). It is encouraging that the membrane association energies are very similar from MARTINI CG (~16 kcal/mol) compared to all-atom simulations (~14–16 kcal/mol). However, the large barrier for dissociation of the toxin tails from the lipid headgroups (an increase in free energy of ~9 kcal/mol going from Z = 1.3 to 0.3 nm) and the metastable extended configuration demonstrate a very different mechanism of permeation. It is important for the continued use and development of CG models to understand the origin of these differences. An obvious contributing factor is the approximate nature of the CG parameterization and thus differences in the CG and all-atom toxin-lipid interactions. In addition, however, we believe the role of water molecules could play an important role. As discussed in the previous section and shown in Fig. 8, there is no deep-water penetration into the lipid tail region in MARTINI CG simulations, in contrast to the considerable penetration of water molecules observed in unbiased and biased all-atom simulations. These penetrating water molecules stabilize the toxin in the lipid tail region, enabling a balance between hydrophilic and hydrophobic interactions in the membrane environment. This not only helps to eliminate the barrier observed for permeation in the CG simulations, it also alters the mechanism by which the toxin permeates. In the CG simulations, the cost of transitioning to the extended conformation, which maintains polar interactions with the headgroup beads on either side of the membrane, is outweighed by the cost of losing polar interactions in the tail region. Other factors, such as the overly rigid bending modulus and increased lipid diffusivity of MARTINI membranes could additionally be contributing factors to the different PMFs and permeation mechanisms (67–69).

CONCLUSIONS

Mycolactone is a complex and multifunctional molecule that targets various structures in the cell and likely influences membrane microdomains. This cytotoxic macrolide is known to play the central role in the progression of Buruli ulcer disease by disrupting multiple cellular functions. Effective diagnostic methods are still missing, partially because of the association of mycolactone with lipidic structures, enabling this lipid-like molecule to hide from tracking agents. Moreover, the association of mycolactone with lipid-carrying moieties could explain how the toxin evades the secondary immune response and travels far from the site of infection. Therefore, understanding the toxin's interactions with lipids, permeation mechanism and localization is important to understand its pathogenesis and to design effective diagnostics. Furthermore, the findings from mycolactone can be extended to other amphipathic molecules to understand host-pathogen interactions in general. Toward this aim, we have presented all-atom and MARTINI CG TTMetaD simulations that characterize the behavior of

two isomers (mycolactone A and B) interacting with a DPPC membrane.

Our all-atom simulations demonstrate a strong association between the toxin and membrane with a free energy of ~14–16 kcal/mol. They also confirm the expected role of hydrophobic-hydrophilic interactions for any amphiphile, with the macrolide ring burying in the lipid tails and the polar toxin tails interacting with lipid headgroups and water. There is a slight but remarkable difference in the energetics of two isomers during the permeation. Comparing to mycolactone B, mycolactone A exhibits a stronger binding affinity and a smaller free energy increase when it flips from one leaflet to the other (Fig. 4 vs. Fig. 5, as well as Fig. 6). This variation can be explained by the structural difference between two isomers: the two tails of mycolactone A can hydrogen bond with each other and collectively coordinate water molecules, allowing it to have a stronger affinity for the membrane and cross the lipid tail region more easily. Our all-atom simulations also demonstrate that water molecules play a critical role in the permeation process. Both isomers are stabilized by coordination to ~2–3 water molecules during permeation.

Although the free energy driving force for membrane insertion is quite similar in the MARTINI CG simulations, the mechanism of permeation of mycolactone B differs substantially from our all-atoms results. The fully stretched configuration is strongly disfavored by both isomers in all-atom simulations but is favored in the MARTINI CG simulations. This discrepancy is consistent with previous publication showing that the extended configuration plays a dominant role in the MARTINI-based permeation mechanism (17). We also observe quite different behavior of toxin hydration in the MARTINI CG simulations: water coordination is disfavored during permeation and there is virtually no deep-water penetration into the MARTINI membrane. Because water molecules penetrating into the lipid tail region will alter the balance between the hydrophilic and hydrophobic interactions, this is expected to contribute to the altered free energy profile and mechanism of permeation.

Although our findings are specific to one lipidic component in membranes, DPPC, this work represents an important step forward in understanding the lipid-specific interactions that undoubtedly play an important role in how mycolactone penetrates host cells, rapidly travels to the endoplasmic reticulum, and subsequently travels far from the site of infection in the host vasculature. They will also play a defining role in the toxin's potential inhibition of membrane microdomain formation. How the toxin interacts with different lipids and how it localizes to different membrane regions and leaflets will strongly influence these processes. These are the processes we seek to understand. Given the mechanistic discrepancies presented herein, it is unlikely that the MARTINI-based CG models will be capable of delineating lipid-specific interactions

with fidelity. Thus, this work points to the importance of using all-atom simulations to further probe lipid trafficking processes in which lipid-specific interactions are important. It also suggests ways in which MARTINI-based CG models could be improved (e.g., by focusing on water-enriched membrane interactions). Our future work will focus on heterogeneous membranes representative of the plasma membrane and endoplasmic reticulum as well as the role of curvature and lipid composition.

SUPPORTING MATERIAL

Supporting Material can be found online at https://doi.org/10.1016/j.bpj.2019.05.012.

AUTHOR CONTRIBUTIONS

J.M.J.S. designed the research. F.A. and R.S. performed the simulations. F.A., R.S., and J.M.J.S. performed the analysis. All authors contributed to writing the article.

ACKNOWLEDGMENTS

REFERENCES

1. George, K. M., D. Chatterjee, …, P. L. Small. 1999. Mycolactone: a polyketide toxin from Mycobacterium ulcerans required for virulence. *Science.* 283:854–857.

2. Walsh, D. S., F. Portaels, and W. M. Meyers. 2011. Buruli ulcer: advances in understanding Mycobacterium ulcerans infection. *Dermatol. Clin.* 29:1–8.

3. Chany, A. C., C. Tresse, …, N. Blanchard. 2013. History, biology and chemistry of Mycobacterium ulcerans infections (Buruli ulcer disease). *Nat. Prod. Rep.* 30:1527–1567.

4. Marsollier, L., P. Brodin, …, S. T. Cole. 2007. Impact of Mycobacterium ulcerans biofilm on transmissibility to ecological niches and Buruli ulcer pathogenesis. *PLoS Pathog.* 3:e62.

5. Hall, B., and R. Simmonds. 2014. Pleiotropic molecular effects of the Mycobacterium ulcerans virulence factor mycolactone underlying the cell death and immunosuppression seen in Buruli ulcer. *Biochem. Soc. Trans.* 42:177–183.

6. Sarfo, F. S., R. Phillips, …, R. E. Simmonds. 2016. Recent advances: role of mycolactone in the pathogenesis and monitoring of Mycobacterium ulcerans infection/Buruli ulcer disease. *Cell. Microbiol.* 18:17–29.

7. Baron, L., A. O. Paatero, …, C. Demangel. 2016. Mycolactone subverts immunity by selectively blocking the Sec61 translocon. *J. Exp. Med.* 213:2885–2896.

8. Hall, B. S., K. Hill, …, R. E. Simmonds. 2014. The pathogenic mechanism of the Mycobacterium ulcerans virulence factor, mycolactone, depends on blockade of protein translocation into the ER. *PLoS Pathog.* 10:e1004061.

9. McKenna, M., R. E. Simmonds, and S. High. 2016. Mechanistic insights into the inhibition of Sec61-dependent co- and post-translational translocation by mycolactone. *J. Cell Sci.* 129:1404–1415.

10. Marion, E., O. R. Song, …, P. Brodin. 2014. Mycobacterial toxin induces analgesia in buruli ulcer by targeting the angiotensin pathways. *Cell.* 157:1565–1576.

11. Song, O. R., H. B. Kim, …, P. Brodin. 2017. A bacterial toxin with analgesic properties: hyperpolarization of DRG neurons by mycolactone. *Toxins (Basel).* 9:E227.

12. Leung, D. W., and M. K. Rosen. 2005. The nucleotide switch in Cdc42 modulates coupling between the GTPase-binding and allosteric equilibria of Wiskott-Aldrich syndrome protein. *Proc. Natl. Acad. Sci. USA.* 102:5685–5690.

13. Padrick, S. B., L. K. Doolittle, …, M. K. Rosen. 2011. Arp2/3 complex is bound and activated by two WASP proteins. *Proc. Natl. Acad. Sci. USA.* 108:E472–E479.

14. Nitenberg, M., A. Bénarouche, …, A. P. Girard-Egrot. 2018. The potent effect of mycolactone on lipid membranes. *PLoS Pathog.* 14:e1006814.

15. Nicolson, G. L. 2014. The fluid-mosaic model of membrane structure: still relevant to understanding the structure, function and dynamics of biological membranes after more than 40 years. *Biochim. Biophys. Acta.* 1838:1451–1466.

16. Lindner, R., and H. Y. Naim. 2009. Domains in biological membranes. *Exp. Cell Res.* 315:2871–2878.

17. López, C. A., C. J. Unkefer, …, S. Gnanakaran. 2018. Membrane perturbing properties of toxin mycolactone from Mycobacterium ulcerans. *PLoS Comput. Biol.* 14:e1005972.

18. Demangel, C., and S. High. 2018. Sec61 blockade by mycolactone: a central mechanism in Buruli ulcer disease. *Biol. Cell.* 110:237–248.

19. Guarner, J. 2018. Buruli ulcer: review of a neglected skin mycobacterial disease. *J. Clin. Microbiol.* 56:e01507–e01517.

20. World Health Organization. 2017. Buruli ulcer (Mycobacterium Ulcerans Infection). WHO, Geneva, Switzerland.

21. Converse, P. J., E. L. Nuermberger, …, J. H. Grosset. 2011. Treating Mycobacterium ulcerans disease (Buruli ulcer): from surgery to antibiotics, is the pill mightier than the knife? *Future Microbiol.* 6:1185–1198.

22. Almeida, D. V., T. F. Omansen, …, E. L. Nuermberger. 2019. Oxazolidinones can replace clarithromycin in combination with rifampin in a mouse model of buruli ulcer. *Antimicrob. Agents Chemother.* 63:e02171–02218.

23. Omansen, T. F., D. Almeida, …, E. L. Nuermberger. 2019. High-dose rifamycins enable shorter oral treatment in a murine model of Mycobacterium ulcerans disease. *Antimicrob. Agents Chemother.* 63:e01478–01518.

24. Converse, P. J., D. V. Almeida, …, E. L. Nuermberger. 2018. Shorter-course treatment for Mycobacterium ulcerans disease with high-dose rifamycins and clofazimine in a mouse model of Buruli ulcer. *PLoS Negl. Trop. Dis.* 12:e0006728.

25. Converse, P. J., S. Tyagi, …, J. H. Grosset. 2015. Efficacy of rifampin plus clofazimine in a murine model of Mycobacterium ulcerans disease. *PLoS Negl. Trop. Dis.* 9:e0003823.

26. Converse, P. J., Y. Xing, …, Y. Kishi. 2014. Accelerated detection of mycolactone production and response to antibiotic treatment in a mouse model of Mycobacterium ulcerans disease. *PLoS Negl. Trop. Dis.* 8:e2618.

27. Zhang, T., S. Y. Li, …, E. L. Nuermberger. 2013. Rapid, serial, noninvasive assessment of drug efficacy in mice with autoluminescent Mycobacterium ulcerans infection. *PLoS Negl. Trop. Dis.* 7:e2598.

28. Sarfo, F. S., P. J. Converse, …, J. H. Grosset. 2013. Microbiological, histological, immunological, and toxin response to antibiotic treatment in the mouse model of Mycobacterium ulcerans disease. *PLoS Negl. Trop. Dis.* 7:e2101.

29. Almeida, D. V., P. J. Converse, …, J. H. Grosset. 2013. Bactericidal activity does not predict sterilizing activity: the case of rifapentine in the murine model of Mycobacterium ulcerans disease. *PLoS Negl. Trop. Dis.* 7:e2085.

30. Narh, C. A., L. Mosi, …, D. K. de Souza. 2014. Genotyping tools for *Mycobacterium ulcerans*-drawbacks and future prospects. *Mycobact. Dis.* 4:1000149.

31. Dangy, J. P., N. Scherr, …, G. Pluschke. 2016. Antibody-mediated neutralization of the exotoxin mycolactone, the main virulence factor produced by Mycobacterium ulcerans. *PLoS Negl. Trop. Dis.* 10:e0004808.

32. Snyder, D. S., and P. L. Small. 2003. Uptake and cellular actions of mycolactone, a virulence determinant for Mycobacterium ulcerans. *Microb. Pathog.* 34:91–101.

33. Kubicek-Sutherland, J. Z., D. M. Vu, …, H. Mukundan. 2019. Understanding the significance of biochemistry in the storage, handling, purification, and sampling of amphiphilic mycolactone. *Toxins (Basel).* 11:E202.

34. Wang, J., R. M. Wolf, …, D. A. Case. 2004. Development and testing of a general amber force field. *J. Comput. Chem.* 25:1157–1174.

35. Wang, J., W. Wang, …, D. A. Case. 2006. Automatic atom type and bond type perception in molecular mechanical calculations. *J. Mol. Graph. Model.* 25:247–260.

36. Huang, L., and B. Roux. 2013. Automated force field parameterization for nonpolarizable and polarizable atomic models based on ab initio target data. *J. Chem. Theory Comput.* 9:3543–3556.

37. Case, D. A., T. E. Cheatham, III, …, R. J. Woods. 2005. The Amber biomolecular simulation programs. *J. Comput. Chem.* 26:1668–1688.

38. Jämbeck, J. P., and A. P. Lyubartsev. 2012. Derivation and systematic validation of a refined all-atom force field for phosphatidylcholine lipids. *J. Phys. Chem. B.* 116:3164–3179.

39. Jorgensen, W. L., J. Chandrasekhar, …, M. L. Klein. 1983. Comparison of simple potential functions for simulating liquid water. *J. Chem. Phys.* 79:926–935.

40. Wu, E. L., X. Cheng, …, W. Im. 2014. CHARMM-GUI Membrane builder toward realistic biological membrane simulations. *J. Comput. Chem.* 35:1997–2004.

41. Nagle, J. F., and S. Tristram-Nagle. 2000. Structure of lipid bilayers. *Biochim. Biophys. Acta.* 1469:159–195.

42. Dickson, C. J., B. D. Madej, …, R. C. Walker. 2014. Lipid14: the amber lipid force field. *J. Chem. Theory Comput.* 10:865–879.

43. Bussi, G., D. Donadio, and M. Parrinello. 2007. Canonical sampling through velocity rescaling. *J. Chem. Phys.* 126:014101.

44. Berendsen, H. J. C., J. P. M. Postma, …, J. R. Haak. 1984. Molecular dynamics with coupling to an external bath. *J. Chem. Phys.* 81:3684–3690.

45. Essmann, U., L. Perera, …, L. G. Pedersen. 1995. A smooth particle mesh Ewald method. *J. Chem. Phys.* 103:8577–8593.

46. Hess, B., H. Bekker, …, J. G. E. M. Fraaije. 1997. LINCS: a linear constraint solver for molecular simulations. *J. Comput. Chem.* 18:1463–1472.

47. Abraham, M. J., T. Murtola, …, E. Lindahl. 2015. GROMACS: high performance molecular simulations through multi-level parallelism from laptops to supercomputers. *SoftwareX.* 1–2:19–25.

48. Tribello, G. A., M. Bonomi, …, G. Bussi. 2014. PLUMED 2: new feathers for an old bird. *Comput. Phys. Commun.* 185:604–613.

49. Laio, A., and M. Parrinello. 2002. Escaping free-energy minima. *Proc. Natl. Acad. Sci. USA.* 99:12562–12566.

50. Laio, A., and F. L. Gervasio. 2008. Metadynamics: a method to simulate rare events and reconstruct the free energy in biophysics, chemistry and material science. *Rep. Prog. Phys.* 71:126601.

51. Barducci, A., M. Bonomi, and M. Parrinello. 2011. Metadynamics. *WIRES Comput. Mol. Sci.* 1:826–843.

52. Sun, R., J. F. Dama, …, G. A. Voth. 2016. Transition-tempered metadynamics is a promising tool for studying the permeation of drug-like molecules through membranes. *J. Chem. Theory Comput.* 12:5157–5169.

53. Sun, R., O. Sode, …, G. A. Voth. 2017. Simulating protein mediated hydrolysis of ATP and other nucleoside triphosphates by combining QM/MM molecular dynamics with advances in metadynamics. *J. Chem. Theory Comput.* 13:2332–2341.

54. Barducci, A., G. Bussi, and M. Parrinello. 2008. Well-tempered metadynamics: a smoothly converging and tunable free-energy method. *Phys. Rev. Lett.* 100:020603.

55. Dama, J. F., M. Parrinello, and G. A. Voth. 2014. Well-tempered metadynamics converges asymptotically. *Phys. Rev. Lett.* 112:240602.

56. Dama, J. F., G. Rotskoff, …, G. A. Voth. 2014. Transition-tempered metadynamics: robust, convergent metadynamics via on-the-fly transition barrier estimation. *J. Chem. Theory Comput.* 10:3626–3633.

57. E, W., W. Ren, and E. Vanden-Eijnden. 2007. Simplified and improved string method for computing the minimum energy paths in barrier-crossing events. *J. Chem. Phys.* 126:164103.

58. Sun, R., Y. Han, …, G. A. Voth. 2018. Molecular transport through membranes: accurate permeability coefficients from multidimensional potentials of mean force and local diffusion constants. *J. Chem. Phys.* 149:072310.

59. Monticelli, L., S. K. Kandasamy, …, S. J. Marrink. 2008. The MARTINI coarse-grained force field: extension to proteins. *J. Chem. Theory Comput.* 4:819–834.

60. Wassenaar, T. A., H. I. Ingólfsson, …, S. J. Marrink. 2015. Computational lipidomics with insane: a versatile tool for generating custom membranes for molecular simulations. *J. Chem. Theory Comput.* 11:2144–2155.

61. van Eerden, F. J., D. H. de Jong, …, S. J. Marrink. 2015. Characterization of thylakoid lipid membranes from cyanobacteria and higher plants by molecular dynamics simulations. *Biochim. Biophys. Acta.* 1848:1319–1330.

62. Javanainen, M., H. Martinez-Seara, and I. Vattulainen. 2017. Excessive aggregation of membrane proteins in the Martini model. *PLoS One.* 12:e0187936.

63. Risselada, H. J., and S. J. Marrink. 2008. The molecular face of lipid rafts in model membranes. *Proc. Natl. Acad. Sci. USA.* 105:17367–17372.

64. Marrink, S. J., A. H. de Vries, and A. E. Mark. 2004. Coarse grained model for semiquantitative lipid simulations. *J. Phys. Chem. B.* 108:750–760.

65. Winger, M., D. Trzesniak, …, W. F. van Gunsteren. 2009. On using a too large integration time step in molecular dynamics simulations of coarse-grained molecular models. *Phys. Chem. Chem. Phys.* 11:1934–1941.

66. Park, S., A. H. Beaven, …, W. Im. 2015. How tolerant are membrane simulations with mismatch in area per lipid between leaflets? *J. Chem. Theory Comput.* 11:3466–3477.

67. Venable, R. M., H. I. Ingólfsson, …, R. W. Pastor. 2017. Lipid and peptide diffusion in bilayers: the saffman-delbrück model and periodic boundary conditions. *J. Phys. Chem. B.* 121:3443–3457.

68. Stachura, S., and G. R. Kneller. 2014. Anomalous lateral diffusion in lipid bilayers observed by molecular dynamics simulations with atomistic and coarse-grained force fields. *Mol. Simul.* 40:245–250.

69. May, E. R., A. Narang, and D. I. Kopelevich. 2007. Role of molecular tilt in thermal fluctuations of lipid membranes. *Phys. Rev. E Stat. Nonlin. Soft Matter Phys.* 76:021913.